

RESEARCH ARTICLE

10.1002/2016JB013658

Key Points:

- The coefficient of friction of drained, water-saturated montmorillonite ranges from 0.10 at low effective normal stress to 0.28 at 600 MPa
- Water reduces the friction of montmorillonite to less than 20% of dry friction at low stress and around 50% of dry friction at 600 MPa
- We see no plastic limit to shear strength in water-saturated montmorillonite at effective normal stress up to 600 MPa

Correspondence to:

C. A. Morrow,
cmorrow@usgs.gov

Citation:

Morrow, C. A., D. E. Moore, and D. A. Lockner (2017), Frictional strength of wet and dry montmorillonite, *J. Geophys. Res. Solid Earth*, 122, doi:10.1002/2016JB013658.

Received 17 OCT 2016

Accepted 11 APR 2017

Accepted article online 17 APR 2017

Frictional strength of wet and dry montmorillonite

C. A. Morrow¹ , D. E. Moore¹, and D. A. Lockner¹ ¹U.S. Geological Survey, Menlo Park, California, USA

Abstract Montmorillonite is a common mineral in fault zones, and its low strength relative to other common gouge minerals is important in many models of fault rheology. However, the coefficient of friction, μ , varies with degree of saturation and is not well constrained in the literature due to the difficulty of establishing fully drained or fully dried states in the laboratory. We measured μ of both saturated and oven-dried montmorillonite at normal stresses up to 700 MPa. Care was taken to shear saturated samples slowly enough to avoid pore fluid overpressure. For saturated samples, μ increased from 0.10 to 0.28 with applied effective normal stress, while for dry samples μ decreased from 0.78 to 0.45. The steady state rate dependence of friction, $(a - b)$, was positive, promoting stable sliding. The wide disparity in reported frictional strengths can be attributed to experimental procedures that promote differing degrees of partial saturation or overpressured pore fluid conditions.

Plain Language Summary Montmorillonite is a common mineral in fault zones, and its low strength relative to other common fault minerals is important in many models of fault rheology. However, the coefficient of friction varies with degree of saturation and is not well constrained in the literature due to the difficulty of establishing fully drained or fully dried states in the laboratory. In this study, the coefficient of friction, μ , of both saturated and oven-dried montmorillonite was carefully measured in order to avoid pore fluid overpressure. For saturated samples, μ increased from 0.10 to 0.28 with applied effective normal stress, while for dry samples μ decreased from 0.78 to 0.45. The steady state rate dependence of friction, $(a - b)$, was positive, promoting stable sliding. The wide disparity in reported frictional strengths can be attributed to experimental procedures that promote differing degrees of partial saturation or overpressured pore fluid conditions.

1. Introduction

The coefficient of friction of the weak phyllosilicate mineral montmorillonite has been a topic of particular interest in earthquake research ever since *Lachenbruch and Sass* [1980] concluded that a fault frictional strength of 0.2 or less would satisfy the heat flow paradox along the San Andreas fault. Montmorillonite is one of the weakest minerals commonly found in fault zones and satisfies the *Lachenbruch and Sass* [1980] constraint under certain conditions. It is a low-temperature phyllosilicate, generally transitioning to mixed layer montmorillonite/illite and then pure illite above 120 to 150°C. For typical geothermal gradients, montmorillonite could be an important fault zone mineral phase to depths of 4 to 5 km. Different researchers have employed a variety of techniques to measure dry and/or partially to fully saturated frictional strengths of both Na- and Ca-montmorillonite. A partial list (chronologically) includes *Warkentin and Yong* [1962], *Summers and Byerlee* [1977a, 1977b], *Wang et al.* [1980], *Lupini et al.* [1981], *Shimamoto and Logan* [1981], *Morrow et al.* [1982, 1992, 2000], *Bird* [1984], *Logan and Rauenzahn* [1987], *Saffer et al.* [2001], *Saffer and Marone* [2003], *Brown et al.* [2003], *Moore and Lockner* [2007], *Takahashi et al.* [2007], *Ikari et al.* [2007], *Tembe et al.* [2010], *Behnsen and Faulkner* [2012, 2013], *Haines et al.* [2013], and *Carpenter et al.* [2016]. *Moore and Lockner* [2007] point out that inconsistencies in the published data on montmorillonite are often due to differences in saturation state or to uncertainty in the true effective pressure acting on a sample, particularly during undrained or partially drained conditions. These difficulties arise in part because montmorillonite is an expandable clay that typically takes on one to three layers of water in the interlayer spaces. In addition, it has a very high specific surface area, and each crystal surface can adsorb multiple layers of water (as many as six at saturation [*Hagymassy et al.*, 1969; *Ormerod and Newman*, 1983; *Sakuma*, 2013]). Moreover, montmorillonite has extremely low permeability in the range of 10^{-20} to 10^{-22} m² at the pressures of interest (0 to 200 MPa) in crustal geophysical studies [*Morrow et al.*, 1984]. This low permeability slows the attainment of fluid pressure equilibrium, as described by *Wang* [2011]. For these reasons, we have undertaken a systematic study of both oven-dry and wet montmorillonite with care taken to establish fully dry or fully drained

conditions. We have also extended the range of effective normal stress, σ_{neff} , to 700 MPa, well above the pressure range of previous studies. Since smectite clays are low-temperature phyllosilicate minerals, they are unlikely to occur naturally at the highest normal stresses used in this study. Our motivation for spanning such a wide pressure range is based on the fact that water has a profound effect on the frictional properties of montmorillonite, reducing strength by as much as 80%. *Moore and Lockner [2007]* argue that this weakening is due to lubrication of clay platelets by thin films of adsorbed water. *Israelachvili et al. [1988]* demonstrated experimentally that adsorbed water layers between mica sheets can be expelled by increased normal stress, resulting in increased shear strength. In the current study, we measure the strengthening of wet montmorillonite at high normal stress where lubricating water films are increasingly expelled. We find that even at the highest pressures tested, water-saturated montmorillonite has only about half the frictional strength of dried montmorillonite. Additionally, *Saffer et al. [2001]* suggested that with increasing normal stress a transition occurs in montmorillonite from frictional (normal stress-dependent) shear strength to constant shear strength that is insensitive to normal stress. However, at effective normal stress up to 600 MPa, we see no evidence for such a plastic limit in room temperature, water-saturated montmorillonite strength if sufficient care is taken to maintain fully drained conditions. Instead, what is reported as a plastic limit is more likely a transition from a partially saturated to an overpressured state due to compaction in poorly drained samples.

Microfabric evolution of fault gouge has been studied by numerous authors, including, for example, *Riedel [1929]*, *Mandl et al. [1977]*, *Byerlee et al. [1978]*, *Logan et al. [1979]*, *Lupini et al. [1981]*, *Chester and Logan [1986]*, *Rutter et al. [1986]*, *Logan and Rauenzahn [1987]*, *Biegel et al. [1989]*, *Moore et al. [1989]*, *Moore and Byerlee [1991]*, *Beeler et al. [1996]*, *Tembe et al. [2010]*, and *Haines et al. [2013]*. For Coulomb materials with frictional strength that increases with σ_{neff} , failure occurs on planes that are oblique to the plane of maximum shear stress [*Byerlee and Savage, 1992; Savage et al., 1996*] and initial loading typically involves development of crosscutting Riedel shears [*Moore et al., 1989; Haines et al., 2013*]. Stress-strain failure curves can be divided into two types. After an initial, rapid stress increase, many samples attain a peak stress followed by weakening to a residual, steady state stress. *Haines et al. [2013]* associate Riedel shear development with the rapid early compaction and attainment of this peak stress. Other samples do not display a peak in stress but rather undergo a monotonic stress rise to the residual stress. In soil mechanics, the residual stress level is associated with a critical void ratio e_{cr} ($e = \phi/(1 - \phi)$, where ϕ is porosity). Underconsolidated samples that undergo a monotonic increase in stress begin with a void ratio greater than e_{cr} and steadily compact until the critical void ratio is attained. Samples that undergo a peak in stress are initially overconsolidated ($e < e_{cr}$) and dilate until attaining residual strength.

Examples of underconsolidated and overconsolidated samples are found in *Haines et al. [2013]*, their Figures 3a (underconsolidated) and 3f (overconsolidated). In our experiments, we were careful during initial loading to keep stress below the target σ_{neff} . As a result, nearly all of our samples were underconsolidated. Whether a particular sample is underconsolidated or overconsolidated depends in large part on how the sample is prepared as well as the initial loading history. A commonly used technique is to overpressure a sample to precompact it prior to shearing. Thus, the peak stress or the initial rollover in stress-strain curves that typically occurs at about 1 mm displacement should not be considered a material property but mainly the result of sample preparation and preloading history. The residual strength, however, is attained whether the sample is initially overconsolidated or underconsolidated and represents a stable microstructural configuration. This is the stress state that we attempt to identify in the present study. Consequently, we are not interested in the details of the early microfabric development including Riedel shear or P shear formation. In retrospect, the combination of underconsolidation and choice of gouge thickness contributed to challenges in attaining residual strength levels in the higher σ_{neff} runs.

2. Experimental Procedure

Frictional sliding experiments were performed at room temperature on a commercially available Na-montmorillonite, American Colloid Volclay MPS-1, that has the composition $\text{Na}_{0.3}(\text{Fe}^{+2}, \text{Mg})_{0.3}(\text{Al}, \text{Fe}^{+3})_{1.7} \text{Si}_4\text{O}_{10}(\text{OH})_2 \cdot n\text{H}_2\text{O}$. The goal of the wet experiments is to measure the saturated, fully drained strength of montmorillonite over a wide range of normal stress and to see how mechanical expulsion of adsorbed water films would reduce lubrication of platelets at high normal stress. Given the low permeability of the clay, we designed a sample geometry and test sequence that would keep internal pore pressure in equilibrium with

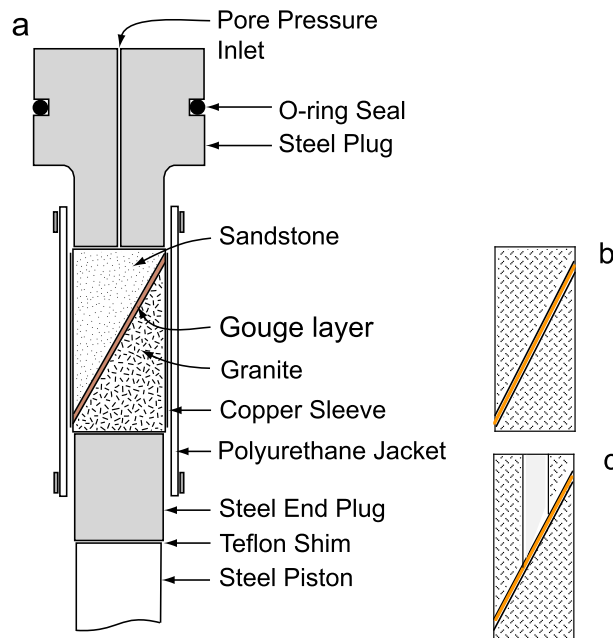


Figure 1. (a) Cross section of the sample assembly with a montmorillonite gouge layer between 30° sawcut sandstone (upper) and granite (lower) driving blocks. (b) Granite upper and lower driving blocks for high normal stress, dry samples. (c) Modified upper granite block with a sandstone core for high normal stress, wet samples.

the external control system. In the past, our standard experimental approach was to apply a 1 mm thick layer of clay paste between the two driving blocks. However, at high normal stress the clay can be pressed into the driving blocks, especially the porous blocks needed to allow good pore fluid communication with the external pore pressure system. To quantify this effect, we examined driving blocks in thin section and found that clay penetration into the sandstone was limited to a few grain diameters (<1 mm). There was no apparent penetration of clay into the granite driving blocks, and there was never extrusion of the clay layer between the driving blocks and jacket material. Nevertheless, to assure that driving blocks would not touch as the gouge layer thinned, especially at high normal stress, we tested thicker clay layers. Accordingly, in the main sequence of tests, 4 g of room dry montmorillonite was placed

between roughened 2.54 cm diameter cylindrical driving blocks containing a 30° sawcut and held together with a 0.013 mm thick copper sleeve (Figure 1a). See *Tembe et al.* [2010] for further details on the sample assembly. We found that 4 g of room dry clay resulted in a layer thickness of approximately 2 mm at the end of each run. While this thick sample guaranteed a continuous clay gouge layer, it also resulted in less total shear strain and slower equilibration of pore pressure transients. We performed two additional dry tests (at 350 and 550 MPa normal stress) using 2 g of clay, resulting in an ending gouge thickness of 0.8 mm (see Appendix A), to measure how additional shear strain would affect the strength observations.

For most experiments, the upper driving block was composed of Berea sandstone (20% porosity) and the lower block was Westerly granite. With this configuration, pore fluids have easy access through the high-permeability sandstone to the external pore pressure system. That is, pore pressure gradients are restricted to the 2 mm width of the gouge layer in contrast to other test geometries where flow to a central port or external boundary would result in a flow path of tens of millimeters. A low-porosity material is desirable for the lower block, so that pore fluids do not become trapped and overpressured or underpressured below the gouge layer during shearing. Above 300 MPa confining pressure, Berea sandstone will crush, so for dry samples above this value, solid Westerly granite was used for both driving blocks (Figure 1b). For the higher-pressure water-saturated experiments, a modified upper sliding block was fashioned. This consisted of an outer cylinder of Westerly granite (for strength) glued to a 12.7 mm diameter inner core of Berea sandstone that retained a high-permeability path to the gouge layer (Figure 1c). The result is essentially a Westerly granite driving block with a high-permeability central core.

For dry experiments, the rock assembly was vacuum dried at 150°C for 2 to 3 days before being placed in a latex or polyurethane jacket. Weighing of the clay (initially room dry) before and after vacuum drying showed between 7.2 and 7.9 wt % loss of adsorbed water. Similar tests run by *Ikari et al.* [2007] and *Carpenter et al.* [2016] reported about 11 and 16% weight loss during drying, respectively. For wet experiments, a room dry sample was jacketed and placed in a pressure vessel with a small confining pressure. The sample and pore pressure system were then evacuated for 0.5 h before deionized water was introduced. Confining pressure was increased to the desired pressure, then pore pressure was fixed at 10 MPa and the sample left to equilibrate for a minimum of 14 h. Care was taken to not overconsolidate the samples during pressurization. The

volume and flow rate of the water expelled from the gouge was monitored in order to determine when the pore fluid pressure had equilibrated at the desired test pressure.

Triaxial sliding experiments on both wet and dry samples were conducted at constant effective normal stress ranging from 10 to 700 MPa at room temperature. In the test geometry shown in Figure 1, increasing shear stress on an inclined sawcut is accompanied by an increase in normal stress. Thus, confining pressure was adjusted as needed under computer control, once per second, to maintain constant normal stress. We varied axial shortening rates in decade steps to determine the dependence of friction on sliding velocity. Dry experiments lasted about 20 h at axial shortening rates of 0.01, 0.1, and 1.0 $\mu\text{m/s}$ (sliding times of 20,000, 5000, and 1000 s, respectively). The wet experiments were run more slowly, lasting more than 3 days each, with constant shortening rate segments of 0.01 and 0.1 $\mu\text{m/s}$ (sliding times of 50,000 and 5,000 s, respectively) to maintain pore pressure equilibration between the gouge layer and the external control system. It should be noted that additional shear-enhanced compaction will inevitably occur when the samples are deformed. For the wet samples, the volume of expelled pore water was recorded to help determine whether the gouge layer porosity had equilibrated satisfactorily with each change in sliding velocity. If shearing is conducted too quickly, excess pore pressure can build up in the gouge layer, causing the true effective normal stress to be less than what is measured externally.

In all tests, shear stress was corrected for the decreasing area of contact along the 30° inclined sawcut, as the driving blocks were displaced, and for the shear strength of the latex or polyurethane jacketing material. As sliding proceeded, the jackets would stretch and shear resistance would increase, but by 8 mm slip, shear stress corrections remained less than 1 MPa. See *Tembe et al.* [2010] for additional details on corrections. Axial shortening of the sample column was measured outside the pressure vessel and was corrected for elastic shortening of the piston and sample assembly. Gouge compaction was not measured during the experiments, but upon removal from the pressure vessel, gouge layer thickness was measured whenever possible.

The uncertainty in measured stresses and jacket strength corrections give an accuracy of ± 0.01 for coefficient of friction, and variability in sample preparation gives a repeatability of about ± 0.02 . But in a single experiment, changes in μ (used to determine the velocity dependence parameter ($a - b$)) are known to ± 0.001 because many of the sources of error cancel within a single run. Coefficients of friction were determined at 8 mm of axial displacement at an axial shortening rate of 0.1 $\mu\text{m/s}$ so that the gouge texture had time to evolve. For a 30° inclined fault, fault-parallel slip is ~ 1.155 times the axial shortening. Then, at 8 mm axial shortening, shear strain is 4.6 (assuming a nominal 2 mm thick shear zone). Experimental conditions and results are given in Table 1.

3. Results

3.1. Friction

We report all strength measurements as coefficient of friction

$$\mu = \tau / (\sigma_n - p) \quad (1)$$

resolved on the inclined sawcut surface, where τ is fault-parallel shear stress, σ_n is fault-normal stress, and p is pore pressure. Note that this is different than the tangent to the failure curve, commonly used in defining the internal coefficient of friction. Friction results from typical sliding experiments are shown in Figure 2 for both wet and dry samples at representative effective normal stress ($\sigma_{\text{neff}} = \sigma_n - p$). In all tests, the coefficient of friction increased rapidly as deviatoric stress was applied until between 0.5 and 2 mm of axial displacement and thereafter showed a gradual, roughly linear strengthening with slip. This strengthening was greater at higher effective normal stress and also higher for the dry versus wet samples (see Table 1). None of the friction data showed a significant peak stress before shearing commenced [e.g., *Haines et al.*, 2013] indicating that the gouge layer was not overconsolidated at the start of the experiment. Given the limited total slip available in this test geometry, most samples did not reach a residual strength by the end of the experiment, that is, strength that remains constant with continued displacement. Final friction values at 8 mm axial shortening are therefore considered a lower bound of the residual strength. Decade changes in sliding velocity caused small variations in the coefficient of friction (inset, Figure 2b) that are discussed in section 3.2.

Table 1. Description of Samples

$\sigma_{n,eff}$ MPa	State	μ at 8 mm	a-b	Hardening ^a <i>h</i>	Thickness ^b mm	Comments ^c
10	wet	0.091	0.0011		2.6	lead jacket, slide to 5 mm
10	wet	0.119				5 g gouge
10	dry	0.756	0.0053	0.029	3.2	lead jacket, slide to 5 mm
10	dry	0.791				
20	wet	0.107	0.0006	0.003	2.3	
20	dry	0.669	0.0069	0.024	2.8	
50	wet	0.113	0.0004	0.000	2.4	5 g gouge
50	wet	0.113	0.0002	0.002	2.3	
50	dry	0.585	0.0072	0.012	2.0	
50	dry	0.620	0.0096	0.014	1.9	
50	dry	0.579	0.0069	0.014	1.7	
100	wet	0.129	0.0004	0.005	2.4	
100	dry	0.567	0.0049	0.017	1.8	
150	wet	0.164	0.0013	0.013	2.6	
150	wet	0.154	0.0013	0.006	2.0	
150	wet	0.176	0.0010	0.007	1.9	
150	dry	0.542	0.0035	0.017	1.6	
190	wet	0.178	0.0010	0.011	2.0	1 mm thick layer
190	wet	0.190	0.0017	0.003	0.6	1 mm thick layer
190	wet	0.198	0.0019	0.003	0.5	
190	dry	0.491	0.0019	0.020	1.7	
200	wet	0.181	0.0014	0.010	2.0	
250	wet	0.200	0.0023	0.010	2.0	
250	dry	0.460	0.0017	0.032	2.2	
300	wet	0.216	0.0024			lead jacket, slide to 5 mm
300	wet	0.201				
300	dry	0.471	0.0023	0.025	1.8	
350	dry	0.458	0.0024	0.035	1.8	
350	dry	0.538	0.0025	0.016	0.8	wg/wg, 2 g gouge
400	wet	0.242	0.0030	0.018	2.0	wg/wg with ss core
400	dry	0.424	0.0021		1.7	wg/wg driving blocks
450	dry	0.470				wg/wg driving blocks
450	dry	0.458	0.0021	0.034	1.6	wg/wg driving blocks
500	wet	0.257	0.0042	0.026	2.0	wg/wg with ss core
550	dry	0.492		0.054	2.0	wg/wg driving blocks
550	dry	0.475	0.0034	0.036	1.6	wg/wg driving blocks
550	dry	0.558	0.0024	0.023	0.8	wg/wg, 2 g gouge
594	wet	0.274	0.0065	0.029	2.0	wg/wg with ss core
685	dry	0.466	0.0042	0.055	2.0	wg/wg driving blocks

^aStrain hardening rate, *h*, defined in equation (2), with slope measured between 6 and 8 mm axial displacement.

^bClay layer thickness at end of experiment.

^cAll clay layers from 4 g room dry montmorillonite unless otherwise indicated. All driving blocks are one half Westerly granite (wg) and one half Berea sandstone (ss) unless otherwise indicated.

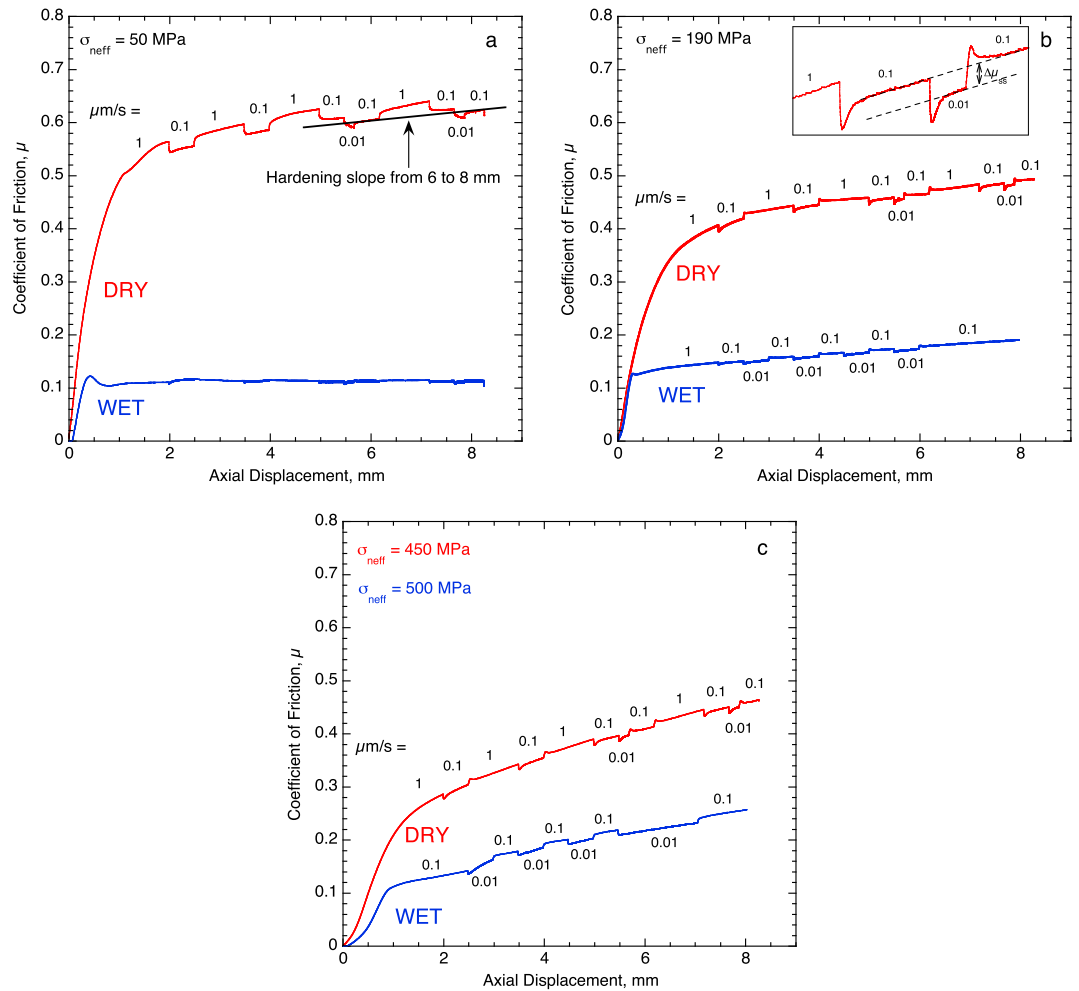


Figure 2. Coefficient of friction as a function of axial displacement for dry and wet montmorillonite samples at three pressure ranges, showing how strain hardening rate increases with increasing normal stress. Axial sliding velocities are indicated in $\mu\text{m/s}$ along the curves. (a) Effective normal stress = 50 MPa. The strain hardening rate, h , reported in Table 1, is determined from the strength slope between 6 and 8 mm. (b) Effective normal stress = 190 MPa. A blowup (inset) of the frictional response of the dry sample to changes in sliding velocity between 7 and 8 mm axial displacement shows how the change in steady state friction, $\Delta\mu_{ss}$, is determined. (c) Effective normal stress = 450 and 500 MPa.

The strain hardening rate is defined as $h = \partial\mu/\partial\gamma$ where γ is shear strain. For final clay thickness t , we approximate shear strain as $\gamma \sim \delta/t$ where δ is fault-parallel slip. Then we approximate the hardening rate as

$$h \approx \Delta\mu/\Delta\gamma. \tag{2}$$

Hardening rates, as determined between 6 and 8 mm displacement, are plotted in Figure 3 and listed in Table 1. For both wet and dry experiments h increases with increasing σ_{neff} . The normal stress dependence is essentially the same for wet and dry runs ($\Delta h/\Delta\sigma_{\text{neff}} = 5.2 \times 10^{-5} \text{ MPa}^{-1}$) with an offset for the dry experiments of 0.015. Since the same trend is observed in both wet and dry series, it cannot be the result of pore fluid effects. The hardening trend is more likely the result of the efficiency of microfabric evolution, grain size reduction, and densification as described, for example, in Haines *et al.* [2013]. Precise determination of these processes is beyond the scope of the present study. However, as seen in Figure 2, based on our data with a maximum slip of 8 mm, we cannot estimate the total slip beyond which strain hardening would cease (especially at higher σ_{neff}). Two additional dry tests were conducted at 350 and 550 MPa normal stress (red crosses in Figure 3) using thinner clay layers as described in Appendix A. By using half the gouge thickness, 8 mm of axial shortening produced about twice the total shear strain ($\gamma \sim 10$). The strain hardening rate was lower for

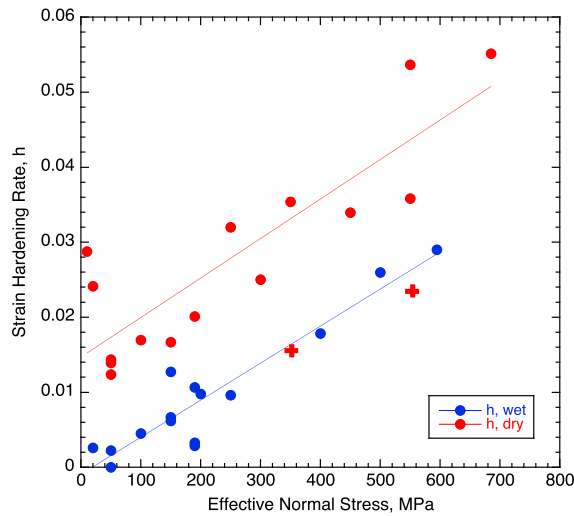


Figure 3. Strain hardening rate, h , for dry and wet samples taken from the slopes of the friction curves between 6 and 8 mm of axial displacement. Lines are least squares fits to the data. Red crosses are for samples with approximately half the layer thickness and therefore twice the shear strain. See Table 1 for values of h .

from 0.8 to around 0.45 between 10 and 700 MPa normal stress, whereas μ of the weaker wet samples gradually increased from 0.10 to 0.28 between 10 and 600 MPa. That is, the dry and wet data sets approach each other with increasing normal stress but do not merge. By 600 MPa effective normal stress, wet strength was still about half of the dry strength. Multiple runs at the same conditions give an indication of repeatability in measuring friction (about ± 0.02). The decrease in μ of the dry samples is more or less complete by 250 MPa. The wet samples, on the other hand, strengthen with increasing stress over the entire pressure range that we tested. The steady increase in wet friction coefficient with increasing σ_{neff} indicates a progressive reduction in the lubricating ability of pore water, similar to pressure-sensitive friction of wet chrysotile [Moore *et al.*, 2004].

The two dry tests on thinner gouge layers (red crosses in Figures 4a and 4b) were notably stronger, showing the effect of doubling the average shear strain (see Appendix A). Since even the thin gouge layers were still strengthening at the end of the tests, we were not able to determine the residual frictional strength of the samples, especially the high normal stress dry samples. Thus, the dry strengths plotted here represent a lower bound on the frictional strength of the clay.

3.2. Sliding Velocity

Changes in sliding velocity caused systematic variations in the coefficient of friction, with instantaneous, transient, and steady state responses, as shown in Figure 2. We will not discuss the transient frictional response that immediately follows each velocity change, displaying a distinctive peak (or trough) and which occurs over a characteristic displacement, d_c . Instead, we report the changes in steady state friction response following the strength transients. By constructing parallel trend lines linking the coefficient of friction during like velocities (see inset, Figure 2b), the change in steady state friction, $\Delta\mu_{ss}$, that is related to changes in velocity can be separated from the irreversible displacement-dependent strengthening represented by h .

The steady state velocity dependence of friction is defined as

$$a - b = \Delta\mu_{ss} / \ln(V_2/V_1), \tag{3}$$

where $\Delta\mu_{ss}$ is the change in steady state friction, and V_1 and V_2 are initial and final sliding velocities. Note that in this definition of $a - b$, steady state friction is not necessarily the same as residual (i.e., constant) friction as discussed above because we remove strain hardening during the measurement of $\Delta\mu_{ss}$. The parameter ($a - b$) is important in models of fault stability in that neutral or rate-strengthening values indicate a tendency for stable sliding, analogous with creep on active faults. The measured ($a - b$) values, plotted in Figure 5, are all positive: increasing slip rate results in increasing strength. Small open symbols are the measured data

these two samples, although it was still positive. With continued strain, dry strength is indeed approaching Byerlee law frictional values [Byerlee 1978] that are not normally associated with phyllosilicates.

Shear stresses and coefficients of friction determined at 8 mm of axial displacement and a sliding velocity of 0.1 $\mu\text{m/s}$ are shown in Figure 4 as a function of effective normal stress for all of the test samples. Dry and wet samples follow distinct trends; shear stress and friction values for the dry samples plot significantly higher than the equivalent wet samples, as observed in Figure 2. The two trends are distinctly nonlinear, particularly at lower pressures, as best seen in the friction plot in Figure 4b. The coefficient of friction of the dry samples decreased

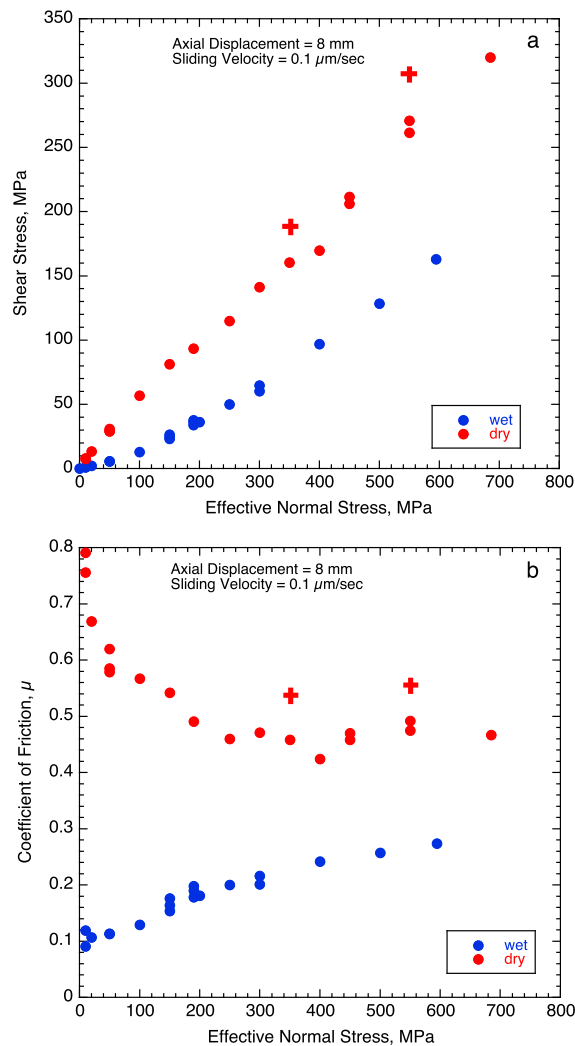


Figure 4. (a) Shear stress and (b) coefficient of friction as a function of effective normal stress for dry and wet samples. Red crosses are for thinner clay layers that have undergone approximately twice the shear strain as the standard samples. Error bars for individual experiments are smaller than the data points.

et al. [2007]. Our determination of wet montmorillonite ($a - b$) is in good agreement with a value of 0.0005 reported by *Tembe et al.* [2010] at $\sigma_{\text{neff}} = 40$ MPa.

4. Discussion

4.1. Friction Mechanisms of Wet Versus Dry Montmorillonite

Frictional strength of montmorillonite and its dependence on normal stress are strongly dependent on whether the sample is dry or wet and, if wet, are functions of saturation state. *Morrow et al.* [2000], *Moore and Lockner* [2004], and *Behnsen and Faulkner* [2012] found that the dry frictional strength of the 2:1 sheet silicate minerals is correlated with the strength of their calculated interlayer, (001), bonds [*Giese* 1978; *Sakuma and Suehara* 2015]. The (001) bond strength is a function of the layer charge and whether or not the mineral is dioctahedral or trioctahedral [*Giese* 1978]. As discussed by *Moore and Lockner* [2004], dioctahedral montmorillonite, with its small layer charge, might be expected to have a dry friction coefficient slightly higher than that of dioctahedral pyrophyllite, which has no layer charge ($\mu \sim 0.4$ at 100 MPa). However, the coefficient of friction of dry montmorillonite at the lowest pressures approaches 0.8. *Kosoglu et al.* [2010] note that when montmorillonite is dried, the platelets tend to form small aggregates in a slightly misaligned,

(between two and four measurements per experiment), and the large filled circles are the averaged values. The average ($a - b$) values of dry samples are largest (0.005 to 0.009) below 50 MPa and decrease to a minimum of around 0.002 at 200–250 MPa before increasing again to 0.004 at 700 MPa. The trend for wet samples was distinctly different, with a much lower ($a - b$) of 0.0017 at low stress, dropping to nearly 0 at 50 MPa and then steadily increasing to more than 0.006 at 600 MPa. The wet and dry values of ($a - b$) overlap in the effective normal stress range 200 to 350 MPa. The velocity dependence of the two data sets is most divergent at effective normal stresses below 200 MPa. Average ($a - b$) of wet and dry samples are plotted as a function of the coefficient of friction, μ , in Figure 5b. Least squares fits to the wet and dry data show that ($a - b$) generally increases with friction.

Although differences between wet and dry ($a - b$) values have been reported in the literature, it is difficult to compare our overall results with other studies, as most have different saturation conditions and focus on normal stresses below 100 MPa. In this normal stress range, our dry montmorillonite values range from ($a - b$) \approx 0.005 to 0.009 and are higher than pure dry montmorillonite values of 0 to 0.004 reported by *Ikari*

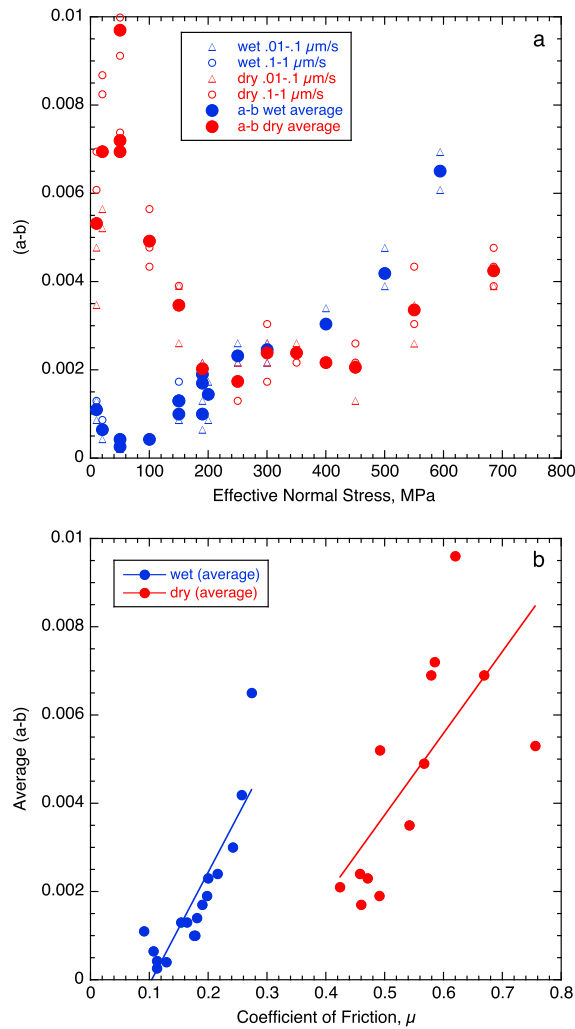


Figure 5. (a) Velocity dependence of friction, $(a - b)$, as a function of effective normal stress for dry and wet samples. Small symbols show measured data; open triangles are slower velocities, and open circles are faster velocities. Large solid symbols indicate average values. (b) Average $(a - b)$ as a function of coefficient of friction, μ .

the data shown here in Figure 4 and additional recent data from the literature. Because most studies concentrate on effective normal stresses below 100 MPa, we have provided an expanded plot of this range in Figure 6b. We discovered that normal stress was plotted incorrectly for the montmorillonite strength data in *Morrow et al.* [1992, Figure 7a] and was subsequently reproduced in *Moore and Lockner* [2007]. Those data are now plotted correctly in Figure 6 and are in close agreement with the current observations.

Figure 6 shows room temperature friction values reported in the literature that span a remarkable range from 0.02 to 0.79. While there is some dependence of μ on effective normal stress, the principal variable controlling μ appears to be water content. The frictional strength of Na-montmorillonite differs slightly from Ca-montmorillonite, a result of the difference in hydration energy of these two cations (see discussion in *Behnen and Faulkner* [2013]), but any subtleties between Na- and Ca-montmorillonite are of secondary importance in understanding the range of friction presented in Figure 6. All values fall below Byerlee's law, [Byerlee, 1978], provided, for reference, as the dashed line in Figure 6a. Indeed, *Byerlee* [1978] noted that phyllosilicates were generally weaker than the framework silicates and other common minerals that he used in formulating his composite strength relation. To understand the frictional properties of montmorillonite, we group data into four general categories comprising a continuum between dry, partially saturated,

subparallel way with some edge-face contacts rather than purely face-face stacking like a deck of cards. Platelets only a few layers thick will curl or flex to fit their surroundings [Güven 1992], and, in consequence, they will not be optimally oriented for easy shear by cleaving through the weak (001) planes. Hence, for this complex edge-face structure, frictional strength exceeds that of the nominal bond strength in the basal plane. During shearing at higher normal stresses, more (001) planes rotate into alignment with the shear planes, resulting in $\mu < 0.8$.

In contrast to dry montmorillonite, the strength of saturated samples is strongly influenced by lubrication from weakly bound structured water layers that separate clay particles and facilitate shear [e.g., *Israelachvili et al.*, 1988]. At higher pressures (and temperatures) this water is expelled and its ability to aid particles in slipping past each other is reduced. This tendency is clearly demonstrated for wet chrysotile [Moore et al., 2004] and has been proposed as a mechanism for high deformation rate strengthening in granitic gouge layers [Sammis et al., 2011].

Figure 6a is a compilation of all published room temperature montmorillonite strength data. It represents an updated version of Figure 11.10 of *Moore and Lockner* [2007], adding

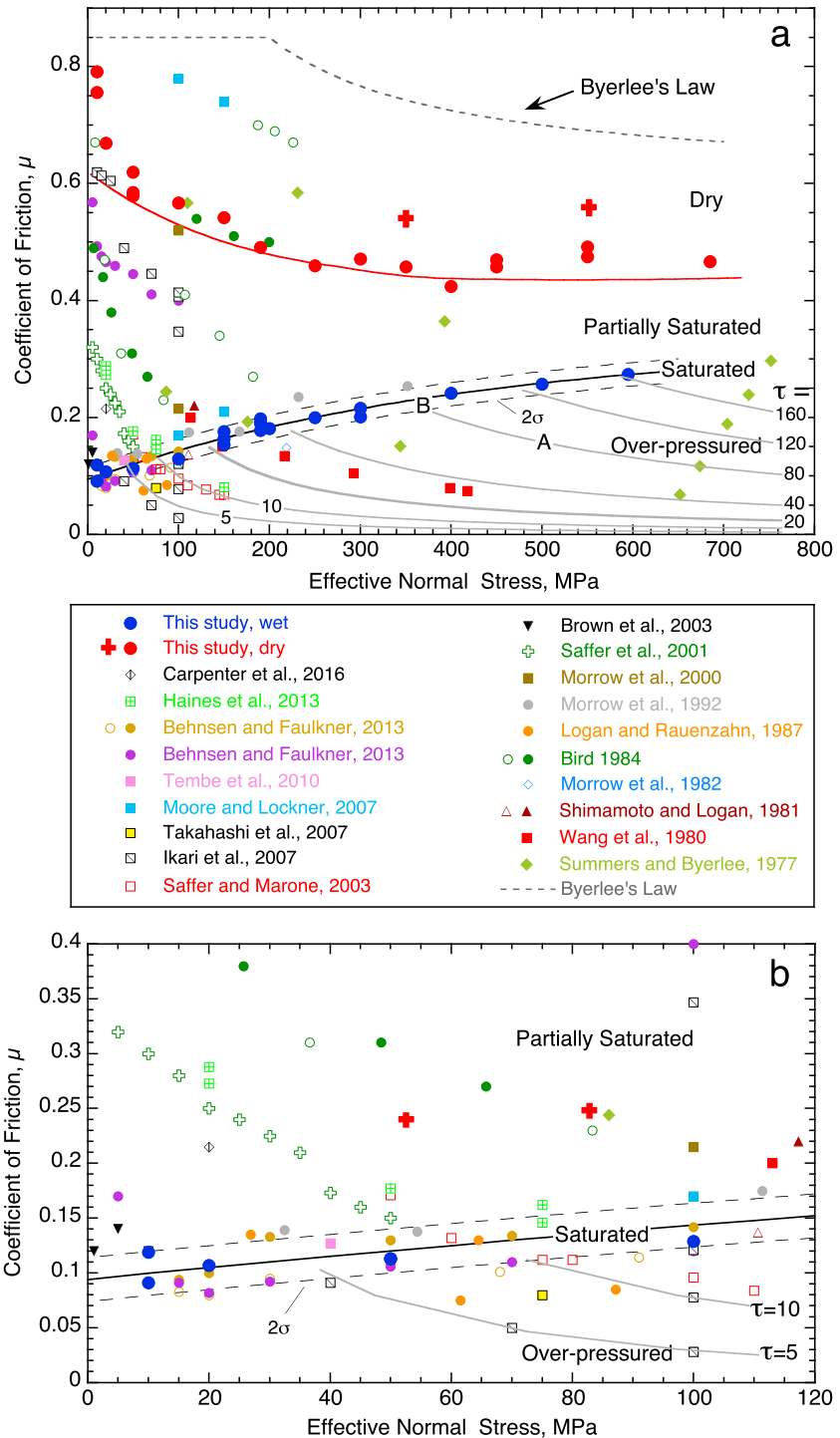


Figure 6. (a) Coefficient of friction of montmorillonite from this study (red and blue circles and red crosses) combined with all available strength measurements from the published literature. This represents an update of a similar plot in *Moore and Lockner* [2007]. Solid symbols denote Na-montmorillonite, and open symbols are Ca-montmorillonite. Byerlee's law (dashed line) is included for reference. Data are grouped into four regions: dry, partially saturated, saturated, and overpressured, according to fluid content. Contours of constant shear stress, τ (MPa), are plotted as grey lines in the overpressured region. (b) Blowup of Figure 6a showing details at low effective normal stress.

saturated, and overpressured, in decreasing order of strength. The four sections of this figure provide a useful guide for establishing the saturation state for other montmorillonite friction data sets not described here.

4.2. Dry Strength of Montmorillonite

Dry samples are those that are treated in some way to remove interlayer and surface-adsorbed water, usually by heating. Many data points cluster near our dry curve, but a few points, both Ca and Na exchange varieties [Moore and Lockner, 2007; Bird, 1984; Summers and Byerlee, 1977a, 1977b], as well as our two samples with thinner gouge layers and correspondingly more shear strain (red crosses), fall well above it. The difference in strength is most likely because many of our samples along the dry curve were still strengthening at 8 mm of displacement. By using a relatively thick gouge layer in our main test series, the total strains are generally less than those achieved in similar studies and tend to end while samples are still strain hardening. By preparing our samples in a consistent manner, our results show an overall reduction in dry friction with increasing effective normal stress that is similar to Byerlee's law although well below it. Identifying a precise value for dry friction is problematic for a hydrophilic mineral such as montmorillonite. Even small amounts of adsorbed water will facilitate intergranular slip and reduce friction. Therefore, the boundary that we have drawn between "dry" and "partially saturated" is only approximate and should be considered a lower bound on dry strength. Natural faults in the earth are rarely, if ever, dry, and friction values associated with this condition are primarily of interest for understanding the mechanisms that control shear strength.

4.3. Partially Saturated Strength of Montmorillonite

Frictional strength in the partially saturated region is strongly dependent on the amount of adsorbed water that provides a lubricating surface on the clay platelets as described by Moore and Lockner [2007] and many other researchers. Note that several studies report on the frictional strength of "room dry" gouge. These might best be described as "room humidity" experiments, having taken on significant water from the atmosphere [e.g., Saffer and Marone, 2003; Ikari et al., 2007; Haines et al., 2013; Kawai et al., 2015]. Such samples would be more correctly considered within the partially saturated region since there is affinity for water both through direct adsorption and through attraction of hydrated counterions [Revil and Lu, 2013]. In drying our starting material, we found approximately 7% weight loss. Ikari et al. [2007] and Carpenter et al. [2016] reported about 11 and 16% weight loss during drying, respectively. In fact, room dry data from Behnsen and Faulkner [2012] and others fall neatly into this partially saturated region. In principle, contours representing the degree of partial saturation could be drawn in this domain given enough information on porosity and water content. Bird [1984] and Ikari et al. [2007] state the weight percent of water in their samples, although from this alone we cannot deduce the percent saturation (which also depends on the void ratio of the clay at a given normal stress and strain). Since porosity is reduced as normal stress increases, the degree of partial saturation should systematically increase in an experiment where the water content is fixed and normal stress is progressively increased. With sufficient reduction in porosity, water will fill all available pore space and the sample will attain a fully saturated condition. Thus, these samples exhibit decreasing friction as the saturation level increases and ultimately intersects the fully saturated curve, as shown in Figure 6. In their room dry experiments, Saffer et al. [2001] proposed a plastic limit to shear strength above around 30 MPa. We see no indication that there is a plastic limit (constant shear strength independent of increasing normal stress) in our fully saturated experiments (see Figure 4a). Under both wet and dry conditions, deformation is always frictional in the sense that shear strength is effective normal stress dependent, even above 600 MPa.

4.4. Fully Drained, Saturated Strength of Montmorillonite

Poroelastic theory typically considers two end member conditions for deformation of saturated rock or geologic material, referred to as drained and undrained. An undrained condition is one in which no pore fluid enters or leaves the sample. In this case, compression of the sample also compresses the trapped pore fluid, resulting in increased pore pressure and a corresponding decrease in σ_{neff} . This case is discussed in the next section. Conversely, a fully drained sample allows free flow of pore fluid and is represented by constant pore pressure such that the measured external pore pressure is the same as pore pressure within the gouge. Several data sets fall within the fully saturated and fully drained region including data from this paper, Morrow et al. [1992], Moore and Lockner [2007], Tembe et al. [2010], and Behnsen and Faulkner [2012, 2013]. In principle, these data should represent a material property of the clay and fall in a narrow band, taking into account the differences in frictional strength between, for example, Na- and Ca-montmorillonite as described

by *Behnsen and Faulkner* [2013], and the data should be reproducible between different laboratories. *Behnsen and Faulkner* [2012] report all friction values just after the early elastic portion of the loading curve transitions into shear sliding in order to avoid strain-hardening effects altogether. Most other studies report friction values under fully developed steady state shearing or residual strength conditions. The solid line plotted in Figure 6 represents a third-order polynomial fit to our measured values with adjacent dashed lines indicating a two standard-deviation confidence interval. The curve represents the frictional strength of room temperature water-saturated montmorillonite clay at a sliding rate of $0.115 \mu\text{m s}^{-1}$ that corresponds to a nominal shear strain rate of $5 \times 10^{-5} \text{s}^{-1}$. This polynomial fit is consistent with data reported in other similar studies carried out under precisely controlled pore pressure conditions. Note that rate dependence given by equation (3) implies increased μ at faster strain rates. For example, if $(a - b) = 0.0043$, a tenfold increase in strain rate would increase μ by 0.01.

4.5. Overpressured Regime

Finally, as discussed in *Moore and Lockner* [2007], steady state sliding strength values cannot technically plot in the overpressured region below the shaded saturated strength curve in Figure 6a. We believe that the most likely reason for reported strength values appearing in this region is that test samples are undrained or partially drained and that shear-enhanced compaction produces pore fluid pressure within the clay layer that is higher than the externally measured pore pressure. In this case, plotted value should be termed apparent effective normal stress $\sigma_{\text{neff}}^{\text{app}}$ and apparent coefficient of friction μ_{app} . The true effective normal stress σ_{neff} and true friction μ lie on the fully saturated strength curve, where a simple construction allows for determination of these parameters as well as the overpressure $p_{\text{excess}} = p_{\text{internal}} - p_{\text{external}}$. For a given stress state with shear stress τ , we have $\mu = \tau/\sigma_{\text{neff}}$ and $\mu_{\text{app}} = \tau/\sigma_{\text{neff}}^{\text{app}} = \tau/(\sigma_{\text{neff}} + p_{\text{excess}})$. Contours of constant τ (gray lines) have been drawn in the overpressured region of Figure 6a. The measured shear stress does not depend on pore pressure, and therefore μ and μ_{app} must lie on the same constant shear stress contour. As an example, a stress state of $[\sigma_{\text{neff}}^{\text{app}}, \mu_{\text{app}}] = [500 \text{ MPa}, 0.16]$ plots at "A" in Figure 6a. This point falls on the $\tau = 80 \text{ MPa}$ contour. In this example, the true stress state within the gouge layer is $[\sigma_{\text{neff}}, \mu] = [360 \text{ MPa}, 0.22]$ and is found at the intersection of the same 80 MPa shear stress contour with the fully saturated strength curve at "B." Excess pore pressure, p_{excess} is then 140 MPa. While the saturated strength curve is concave down, it can be reasonably approximated by a linear function of σ_{neff} with constant slope β of the form

$$\mu = \mu_0 + \beta\sigma_{\text{neff}}. \quad (4)$$

In this case, the following relations hold:

$$\sigma_{\text{neff}} = \frac{-\mu_0 + \sqrt{\mu_0^2 + 4\beta\mu_{\text{app}}\sigma_{\text{neff}}^{\text{app}}}}{2\beta} \quad (5a)$$

$$\mu = \mu_{\text{app}} \frac{\sigma_{\text{neff}}^{\text{app}}}{\sigma_{\text{neff}}} \quad (5b)$$

$$p_{\text{excess}} = \sigma_{\text{neff}}^{\text{app}} - \sigma_{\text{neff}} \quad (5c)$$

A least squares fit to the saturated strength data in Figure 6a yields $\mu_0 = 0.112$ and $\beta = 0.000312 \text{ MPa}^{-1}$.

Undrained experiments subject to increasing pressure are susceptible to the overpressure described above, as are tests run at higher strain rates or with poor communication between the gouge layer and the external pore pressure system. An example of the development of excess pore pressure in a partially drained experiment is presented in Appendix B. This effect was previously noted in experiments by *Wang et al.* [1980] (solid red squares in Figure 6) in which conventional triaxial tests were performed on sealed (undrained) room dry samples. *Saffer et al.* [2001] (open green crosses) and *Saffer and Marone* [2003] (open red squares) tested room dry montmorillonite between $5 \times 5 \text{ cm}$ steel driving blocks in a double-direct shear loading frame. *Ikari et al.* [2007] extended those measurements, in the same apparatus, by controlling starting water content from room dry (11 wt %) to 20 wt % water. Many of the sliding steps in the double-direct shear tests were run at high deformation rates (in excess of $100 \mu\text{m/s}$). In this configuration, free water expelled from the center of

the sample would have to travel more than 2 cm through low-permeability clay to reach a free surface. With increasing normal stress, partially saturated samples would compact, reducing pore space until it was completely filled by the included water; that is, the samples would reach full saturation. At this point, sample strength would lie on the fully saturated curve in Figure 6. This process is consistent with the steady decrease in μ with increasing σ_{neff} observed by *Saffer et al.* [2001] (open green crosses in Figure 6b), where the final 50 MPa measurement had apparently compacted the sample to full saturation. With further increase of applied normal stress, frictional strength for an undrained sample would follow a constant shear stress curve into the overpressured region. We suggest that even though the tests cited here used room dry or partially saturated starting material, samples were compacted at high normal stress to the point that adsorbed water was compressed but had insufficient time to be expelled. If this interpretation is correct, then in addition to reporting anomalously low friction, the rate-dependent effects in those studies may not be measuring a material property of the clay but rather some combination of intrinsic rate dependence combined with poroelastic and diffusion-controlled, partially drained pore-pressure response.

The experiment described in Appendix B illustrates the importance of measuring shear strength of low-permeability materials at strain rates that allow excess pore fluid to equilibrate. Conversely, dilatancy in Coulomb materials can result in reduced internal pore pressure, increased σ_{neff} , and dilatancy hardening [Brace and Martin 1968; Schmitt and Zoback 1992; Lockner and Byerlee 1994]. Pore fluid pressure transients will decay according to the diffusion equation

$$\frac{\partial p}{\partial t} = \alpha \nabla^2 p \quad (6)$$

where α is hydraulic diffusivity. Solutions to equation (6) will depend on the specific sample and fault dimensions. An approximate time constant for transient decay can be estimated by assuming a simple one-dimensional flow path. In this case, a characteristic pressure decay time for a flow path of length L is $T \approx L^2/4\alpha$. Hydraulic diffusivity of a sheared clay layer will decrease with effective normal stress and strain as platelets rearrange and the microstructure and void space evolve. If we assume a representative diffusivity of $\alpha = 10^{-5}$ – 10^{-7} m²/s [i.e., *Wibberley*, 2002], then draining a pressure perturbation in a 2 mm thick clay layer into the adjacent sandstone driving block in our experiments will occur in less than 1 s. For other test geometries where the driving blocks are essentially impermeable, the flow path, either to a central port or to the sample edge, becomes significantly longer. For samples with an average flow path of 2 cm (a common laboratory sample size), pore pressure equilibration may take 100 s or more. Some laboratory geometries can have average flow paths that exceed 4 cm and therefore can expect pressure transients to last well over 1000 s. In this case, deformation tests at slip rates exceeding 10 $\mu\text{m/s}$ may have apparent effective normal stress that is significantly different from the true effective normal stress within the clay test layer.

The choice of appropriate deformation rates is further complicated by shear-enhanced compaction within the clay. When normal stress is applied to the wet clay samples without shearing, they undergo instantaneous compaction followed by decaying time-dependent compaction. However, when a sample is then sheared, additional shear-enhanced compaction will occur that includes strain hardening of the sample as seen in Figure 2. In a fully saturated sample, this additional compaction requires expulsion of pore water. If the strain rate is too rapid, as discussed above, the trapped pore water will become overpressured. Consequently, a balance has to be found, given the particular test geometry, among strain rate, compaction rate, and fluid expulsion that leads to an acceptable overpressure.

5. Summary

With careful attention to saturation state, we have demonstrated that the dry and wet frictional strengths of Na-montmorillonite have distinctly different frictional behavior that depends on applied normal stress. Dry friction decreases with effective normal stress from $\mu \sim 0.8$ at 10 MPa to $\mu \geq 0.45$ at 700 MPa. When samples are water saturated and deformed slowly enough to maintain equilibrium with the external pore pressure system (fully drained), friction increases steadily from $\mu \sim 0.1$ at 10 MPa effective normal stress to $\mu \sim 0.25$ at 600 MPa. The gradual rise in wet friction coefficient can be attributed to mechanical expulsion of

interlayer and surface-adsorbed water that separates the clay platelets and facilitates sliding. The rate dependence of dry and wet frictional strength at a given effective normal stress also differs, particularly below 200 MPa. However, all values of the rate dependence parameter ($a - b$) are positive, implying a tendency for stable sliding at room temperature.

We find that the wide disparity in frictional strength values reported in the literature can be attributed to experimental procedures that promote various degrees of partial saturation or overpressured pore fluid conditions. When comparing different studies, it is important to note how the samples were prepared and how the experiments were conducted. The constitutive law for fully saturated and drained Namontmorillonite at room temperature and constant sliding rate can be reasonably approximated by a linear regression as presented in equation (4), especially if restricted to $\sigma_{\text{neff}} \leq 200$ MPa which would be applicable to most natural situations. Through proper characterization of the degree of partial saturation, a similar constitutive equation could, in principle, be developed that would express shear strength in terms of normal stress and saturation state.

Both the frictional and rate strengthening properties of montmorillonite are important parameters for models of fault behavior. The results reported here provide an important base line for room temperature frictional strength of montmorillonite when sheared under saturated and fully drained conditions. Future work will extend these findings to the evolution of frictional strength at elevated temperature.

Appendix A: Strain Hardening and Development of Residual Strength

With sufficient slip, a sheared clay layer should attain a steady state condition with constant shear strength referred to as residual strength. Ideally, this is the frictional strength value that we measure. In our experiments at higher normal stress, however, samples exhibit strain hardening throughout the deformation. For the main test series, we used 4 g of clay, which resulted in a nominal 2 mm layer thickness. With this geometry we could attain shear strains of $\gamma \sim 5$. In this appendix, we present two additional deformation tests on oven-dry montmorillonite at 350 and 550 MPa normal stress. In this case, the starting material was 2 g of clay, resulting in gouge layers that are half the thickness of the standard test layers, obtaining about twice the strain and ending with higher strength. Results are compared to standard thickness tests in Figure A1. We plot coefficient of friction as a function of shear strain as calculated using the ending layer thickness. The

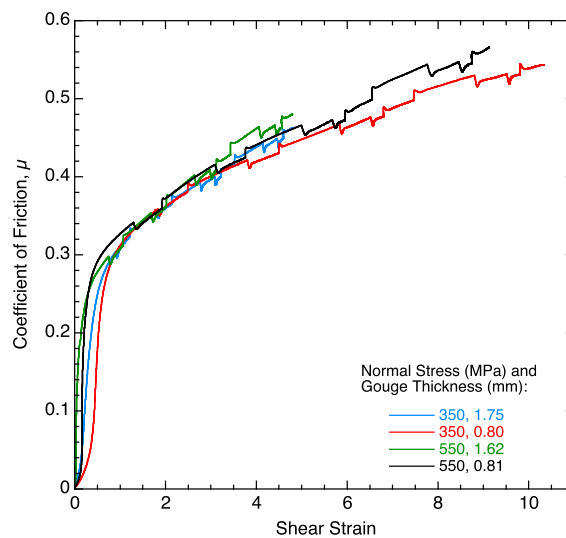


Figure A1. Coefficient of friction of dry montmorillonite tests run at 350 and 550 MPa normal stress to 8 mm axial shortening. Horizontal axis is average shear strain based on ending gouge layer thickness. Standard tests at these pressures had a layer thickness of about 1.7 mm and ended after strains of $\gamma \sim 5$. Two additional tests shown here had a layer thickness of approximately 0.8 mm and attained strains of $\gamma \sim 10$. These thin layer tests achieved higher strength than the corresponding thick layer tests.

periodic fluctuations in strength are caused by decade changes in the imposed slip rate that are used to determine ($a - b$). The friction-strain curves show good agreement until the thick gouge experiments end at $\gamma \sim 5$. This is consistent with our choice to represent hardening rate in terms of average strain rather than total fault slip. If the shear strain localized into a narrow shear band within the gouge layer, then hardening rate should scale with total fault slip and not strain averaged over the layer thickness. Strain hardening rate at the end of the tests is about half the hardening rate measured in the thicker samples (see Figure 3). Still, even with total strain >9 , the samples have not yet achieved steady state conditions. These results confirm that our estimates of dry frictional strength, especially at higher normal stress, should be treated as lower bounds.

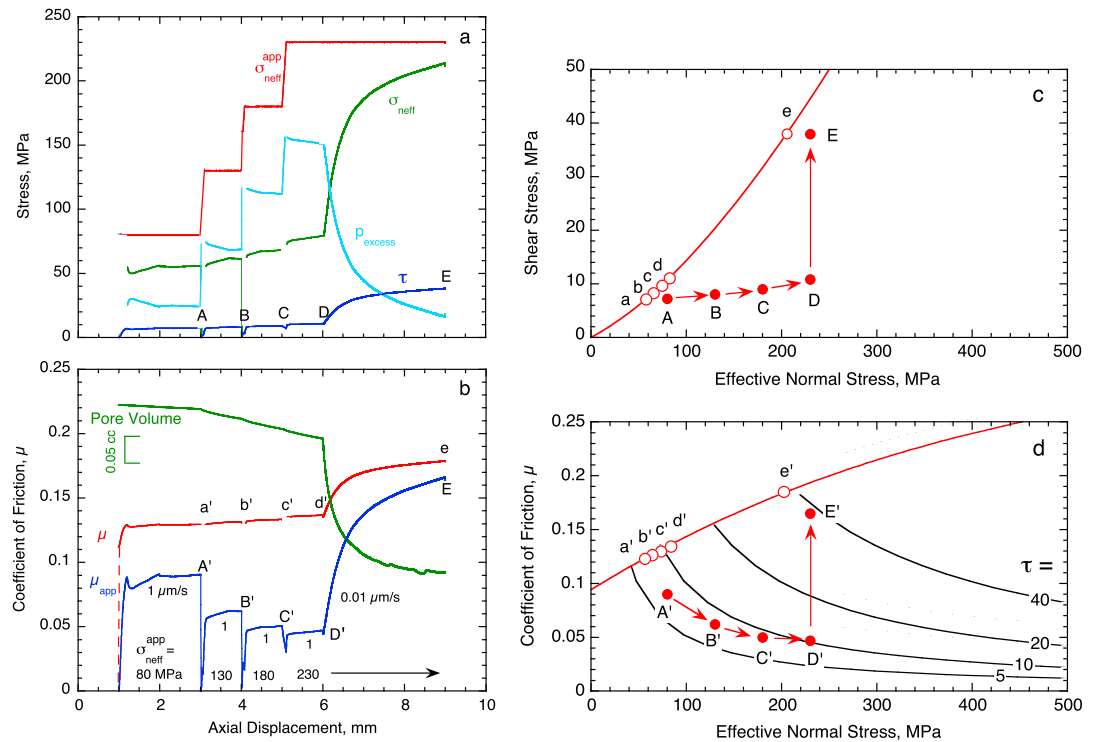


Figure B1. (a) Observed shear stress, τ (dark blue line), for a partially drained experiment in which the externally controlled effective normal stress σ_{neff}^{app} (red line) was periodically increased during the experiment from 80 to 130, 180, and 230 MPa. The axial sliding velocity was fixed at $1 \mu\text{m/s}$ until 6 mm of displacement, where it was decreased to $0.01 \mu\text{m/s}$ allowing excess pore pressure to drain. Points A through E mark the end of each pressure or rate segment on the τ curve. Effective normal stress and excess pore pressure were calculated from equations (5a) and (5c) (green and light blue lines, respectively). (b) Corresponding apparent coefficient of friction, μ_{app} (blue), true coefficient of friction, μ (red, from equation (5b)), and pore volume change (green, note inset scale bar). Apparent friction values (A' through E') and true friction values (a' through e') correspond to shear stress points (A through E) in Figure B1a. (c) Simplified view of shear stress points A through E as a function of effective normal stress. The curved red line corresponds to the saturated frictional strength curve in Figure 6a. Points a through e are obtained by projecting points A through E back to the saturated curve at constant shear stress. (d) Figure B1c replotted as coefficient of friction, with the saturated frictional strength line (red) and constant τ contour lines (black) taken from Figure 6a. True coefficient of friction (points a' through e') is found by shifting apparent coefficient of friction (A' through E') back along constant τ contour lines to the saturated friction curve.

Appendix B: Overpressure Test

We conducted a water-saturated experiment with limited pore fluid connectivity between the sample and the external pore pressure system to produce transient excess pore pressure in the clay gouge. In this experiment we replaced the upper sandstone driving block with a solid granite piece to restrict fluid flow between the clay layer and the external pore pressure system. Permeability of Westerly granite at these run conditions is on the order of 10^{-20} to 10^{-21} m^2 . Given the sample geometry, we would expect that expelling pore water equivalent to 1% of the clay sample volume at a pore pressure difference of, for example, $p_{excess} = 10 \text{ MPa}$ should take approximately 0.1 to 1 days. In the actual experiment, apparent effective normal stress was applied in increasing steps of 80, 130, 180, and 230 MPa as indicated by the red curve in Figure B1a. Throughout the test, external pore pressure was held constant at 10 MPa. The axial shortening rate was $1 \mu\text{m/s}$ until 6 mm, for a duration of 5000 s. Then the rate was reduced to $0.01 \mu\text{m/s}$ for an additional 3 mm shortening at $\sigma_{neff}^{app} = 230 \text{ MPa}$ for a period lasting 3.5 days. The measured shear stress response, τ , is plotted in dark blue. Shear stress was nearly constant for the four initial rapid deformation steps, even though the apparent effective normal stress increased from 80 to 230 MPa.

The actual shear strength and friction coefficient for a fully drained sample that correspond to the applied normal stress and pore pressure are known from the primary experiments in our study. Thus, we can infer the fault zone pore pressure and the excess pressure. Furthermore, if we had ended the experiment at

6 mm displacement, the nearly constant apparent shear strength could be misinterpreted as indicating a plastic yield stress in the clay. However, after the deformation rate was reduced at 6 mm, shear strength steadily increased. The relative change in pore volume (green curve in Figure B1b) indicates the volume of water expelled from the sample at constant external pore pressure. The water loss during the slow deformation step between 6 and 9 mm represents $\sim 10\%$ compaction of the clay layer. Applying equations (5a)–(5c), true effective normal stress (green curve in Figure B1a) and excess pore pressure (light blue curve) are calculated. Relations expressed in equations (5a)–(5c) assume that the clay layer is actively shearing. Thus, gaps appear in the τ and σ_{neff} curves where changes in applied stress result in the shear stress briefly dropping below the yield stress. By the end of the rapid deformation at 6 mm, σ_{neff} is only 37% of $\sigma_{\text{neff}}^{\text{app}}$ and the pore fluid overpressure within the gouge layer is more than 150 MPa. The nearly constant shear strength during rapid shearing before 6 mm deformation results in a decreasing apparent friction μ_{app} (blue curve in Figure B1b). However, the calculated actual friction (red curve) is almost constant since the rise in applied normal stress is nearly matched by a corresponding rise in internal pore pressure. That is, the fault zone is effectively undrained and the Skempton-like poroelastic coefficient relating pore pressure change to normal stress change is 1 (i.e., no change in effective stress in the fault zone).

The five points designated as A through E that represent shear strength at the end of each deformation step in Figure B1a are plotted as a function of effective normal stress, $\sigma_{\text{neff}}^{\text{app}}$ in Figure B1c. The curved red line was taken from the saturated frictional strength curve in Figure 6a and converted into shear stress. Points A through D deviate slightly from a constant shear stress line and indicate partial draining of the pore fluid through the low-permeability granite. When given sufficient time (D to E), excess pore pressure is relieved and the shear stress approaches the saturated, fully drained curve. True shear stress, points a through e, can be found by shifting A through E back horizontally to the saturated line at constant shear stress.

Finally, this same graphical exercise is illustrated for the coefficient of friction in Figure B1d, where μ_{app} points A' through E', taken from Figure B1b, are plotted versus $\sigma_{\text{neff}}^{\text{app}}$. Constant shear stress curves are shown in black, and the red curve is taken from the saturated frictional strength curve in Figure 6a. Points A' through D' deviate slightly from a constant shear stress curve as in the previous figure, indicating partial draining of the pore fluid through the granite. With sufficient time (D' to E'), excess pore pressure is relieved and μ_{app} approaches the saturated curve. Points a' through e', the calculated actual friction from Figure B1b, correspond to the projection of the apparent friction A' through E' back along constant τ contours to the saturated curve.

Acknowledgments

Supporting data for this paper are included in Table 1. Additional data may be obtained from CM (e-mail: cmorrow@usgs.gov). This project was funded by NEHRP. We thank E. Roeloffs, N. Beeler, T. Shimamoto, and B. Carpenter for their helpful reviews. Any use of trade, firm, or product names is for descriptive purposes only and does not imply endorsement by the U.S. Government.

References

- Beeler, N. M., T. E. Tullis, M. L. Blanpied, and J. D. Weeks (1996), Frictional behavior of large displacement experimental faults, *J. Geophys. Res.*, *101*(B4), 8697–8715, doi:10.1029/96JB00411.
- Behnsen, J., and D. R. Faulkner (2012), The effect of mineralogy and effective normal stress on frictional strength of sheet silicates, *J. Struct. Geol.*, *42*, 49–61.
- Behnsen, J., and D. R. Faulkner (2013), Permeability and frictional strength of cation-exchanged montmorillonite, *J. Geophys. Res. Solid Earth*, *118*, 2788–2798, doi:10.1002/jgrb.50226.
- Biegel, R. L., C. G. Sammis, and J. H. Dieterich (1989), The frictional properties of a simulated gouge having a fractal particle distribution, *J. Struct. Geol.*, *11*, 827–846.
- Bird, P. (1984), Hydration-phase diagrams and friction of montmorillonite under laboratory and geologic conditions, with implications for shale compaction, slope stability, and fault gouge, *Tectonophysics*, *107*, 235–260.
- Brace, W. F., and R. J. Martin (1968), A test of the law of effective stress for crystalline rocks of low porosity, *Int. J. Rock Mech. Min. Sci.*, *5*, 415–426.
- Brown, K. M., A. Kopf, M. B. Underwood, and J. L. Weinberger (2003), Compositional and fluid pressure controls on the state of stress on the Nankai subduction thrust: A weak plate boundary, *Earth Planet. Sci. Lett.*, *214*, 589–603.
- Byerlee, J. D. (1978), Friction of rocks, *Pure Appl. Geophys.*, *116*, 615–626.
- Byerlee, J. D., and J. C. Savage (1992), Coulomb plasticity within the fault zone, *Geophys. Res. Lett.*, *19*(23), 2341–2344, doi:10.1029/92GL02370.
- Byerlee, J., V. Mjachkin, R. Summers, and O. Voevoda (1978), Structures developed in fault gouge during stable sliding and stick slip, *Tectonophysics*, *44*, 161–171.
- Carpenter, B. M., M. J. Ikari, and C. Marone (2016), Laboratory observations of time-dependent frictional strengthening and stress relaxation in natural and synthetic fault gouges, *J. Geophys. Res. Solid Earth*, *121*, 1183–1201, doi:10.1002/2015JB012136.
- Chester, F. M., and J. M. Logan (1986), Implications for mechanical properties of brittle faults from observations of the Punchbowl fault zone, California, *Pure Appl. Geophys.*, *124*, 79–106.
- Giese, R. F. (1978), The electrostatic interlayer forces of layer structure minerals, *Clays Clay Miner.*, *28*, 81–86.
- Güven, N. (1992), Molecular aspects of clay-water interactions, in *Clay-Water Interface and Its Rheological Implications*, edited by N. Güven, *Clay Min. Soc. Workshop Lect.*, *4*, 1–79.
- Hagymassy, J., Jr., S. Brunauer, and R. S. Mikhail (1969), Pore structure analysis by water vapor adsorption I. T-curves for water vapor, *J. Colloid Interface Sci.*, *29*, 485–491.

- Haines, S. H., B. Kaproth, C. Marone, D. Saffer, and B. van der Pluijm (2013), Shear zones in clay-rich fault gouge: A laboratory study of fabric development and evolution, *J. Struct. Geol.*, *51*, 206–225, doi:10.1016/j.jsg.2013.01.002.
- Ikari, M., D. Saffer, and C. Marone (2007), Effect of hydration state on the frictional properties of montmorillonite-based fault gouge, *J. Geophys. Res.*, *112*, B06423, doi:10.1029/2006JB004748.
- Israelachvili, J. N., P. M. McGuiggan, and A. M. Homola (1988), Dynamic properties of molecularly thin liquid films, *Science*, *240*, 189–191.
- Kawai, K., H. Sakuma, I. Katayama, and K. Tamura (2015), Frictional characteristics of single and polycrystalline muscovite and influence of fluid chemistry, *J. Geophys. Res. Solid Earth*, *120*, 6209–6218, doi:10.1002/2015JB012286.
- Kosoglu, L. M., B. R. Bickmore, G. M. Filz, and A. S. Madden (2010), Atomic force microscopy method for measuring smectite coefficients of friction, *Clays Clay Miner.*, *58*, 813–820.
- Lachenbruch, A. H., and J. H. Sass (1980), Heat flow and energetics of the San Andreas fault zone, *J. Geophys. Res.*, *85*, 6185–6222, doi:10.1029/JB085iB11p06185.
- Lockner, D. A., and J. D. Byerlee (1994), Dilatancy in hydraulically isolated faults and the suppression of instability, *Geophys. Res. Lett.*, *21*, 2353–2356, doi:10.1029/94GL02366.
- Logan, J. M., and K. A. Rauenzahn (1987), Frictional dependence of gouge mixtures of quartz and montmorillonite on velocity, composition, and fabric, *Tectonophysics*, *144*, 87–108.
- Logan, J. M., M. Friedman, N. Higgs, C. Dengo, and T. Shimamoto (1979), Experimental studies of simulated gouge and their application to studies of natural fault zones, *U.S. Geol. Surv. Open File Rep.*, *79-1239*, 305–343.
- Lupini, J. F., A. E. Skinner, and P. R. Vaughan (1981), The drained residual strength of cohesive soils, *Géotechnique*, *31*, 181–213.
- Mandl, G., L. N. J. de Jong, and A. Maltha (1977), Shear zones in granular material: An experimental study of their structure and mechanical genesis, *Rock Mech.*, *9*, 95–144.
- Moore, D. E., and J. D. Byerlee (1991), Comparative geometry of the San Andreas fault, California, and laboratory fault zones, *Geol. Soc. Am. Bull.*, *103*, 762–774.
- Moore, D. E., and D. A. Lockner (2004), Crystallographic controls on the frictional behavior of dry and water-saturated sheet structure minerals, *J. Geophys. Res.*, *109*, B03401, doi:10.1029/2003JB002582.
- Moore, D. E., and D. A. Lockner (2007), Friction of the smectite clay montmorillonite: A review and interpretation of data, in *The Seismogenic Zone of Subduction Thrust Faults, Margins Theoretical and Experimental Earth Science Series*, vol. 2, edited by T. H. Dixon and C. Moore, pp. 317–345, Columbia Univ. Press, New York.
- Moore, D. E., R. Summers, and J. D. Byerlee (1989), Sliding behavior and deformation textures of heated illite gouge, *J. Struct. Geol.*, *11*(3), 329–342.
- Moore, D. E., D. A. Lockner, H. Tanaka, and K. Iwata (2004), The coefficient of friction of chrysotile gouge at seismogenic depths, in *Serpentine and Serpentinites: Mineralogy, Petrology, Geochemistry, Ecology, Geophysics, and Tectonics*, edited by Ernst, W.G., *Geol. Soc. Am. Internat. Book Ser.*, vol. 8, pp. 525–538.
- Morrow, C., L. Q. Shi, and J. Byerlee (1982), Strain hardening and strength of clay-rich fault gouges, *J. Geophys. Res.*, *87*, 6771–6780, doi:10.1029/JB087iB08p06771.
- Morrow, C., L. Q. Shi, and J. Byerlee (1984), Permeability of fault gouge under confining pressure and shear stress, *J. Geophys. Res.*, *89*, 3193–3200, doi:10.1029/JB089iB05p03193.
- Morrow, C., B. Radney, and J. Byerlee (1992), Frictional strength and the effective pressure law of montmorillonite and illite clays, in *Fault Mechanisms and Transport Properties of Rocks*, edited by B. Evans and T.-F. Wong, pp. 69–88, Elsevier, New York.
- Morrow, C. A., D. E. Moore, and D. A. Lockner (2000), The effect of mineral bond strength and adsorbed water on fault gouge frictional strength, *Geophys. Res. Lett.*, *27*(6), 815–818, doi:10.1029/1999GL008401.
- Ormerod, E. C., and A. C. D. Newman (1983), Water sorption on Ca-saturated clays: II. Internal and external surfaces of montmorillonite, *Clay Miner.*, *18*, 289–299.
- Revil, A., and N. Lu (2013), Unified water isotherms for clayey porous materials, *Water Resour. Res.*, *49*, 5685–5699, doi:10.1002/wrcr.20426.
- Riedel, W. (1929), Zur Mechanik geologischer Brucherscheinungen, *Zentbl. Miner. Geol. Palaeont. Abt.*, *1929B*, 354–368.
- Rutter, E. H., R. H. Maddock, S. H. Hall, and S. H. White (1986), Comparative microstructures of natural and experimentally produced clay bearing fault gouges, *Pure Appl. Geophys.*, *124*, 3–30.
- Saffer, D. M., and C. Marone (2003), Comparison of smectite- and illite-rich gouge frictional properties: Application to the updip limit of the seismogenic zone along subduction megathrusts, *Earth Planet. Sci. Lett.*, *215*, 219–235.
- Saffer, D. M., K. M. Frye, C. Marone, and K. Mair (2001), Laboratory results indicating complex and potentially unstable frictional behavior of smectite clay, *Geophys. Res. Lett.*, *28*, 2297–2300, doi:10.1029/2001GL012869.
- Sakuma, H. (2013), Adhesion energy between mica surfaces: Implications for the frictional coefficient under dry and wet conditions, *J. Geophys. Res. Solid Earth*, *118*, 6066–6075, doi:10.1002/2013JB010550.
- Sakuma, H., and S. Suehara (2015), Interlayer bonding energy of layered minerals: Implication for the relationship with friction coefficient, *J. Geophys. Res. Solid Earth*, *120*, 2212–2219, doi:10.1012/2015JB011900.
- Sammis, C. G., D. A. Lockner, and Z. Reches (2011), The role of adsorbed water on the friction of a layer of submicron particles, *Pure Appl. Geophys.*, *168*, 2325–2334.
- Savage, J. C., D. A. Lockner, and J. D. Byerlee (1996), Failure of laboratory fault models in triaxial tests, *J. Geophys. Res.*, *101*(B10), 22,215–22,224, doi:10.1029/96JB02094.
- Schmitt, D. R., and M. D. Zoback (1992), Diminished pore pressure in low porosity rock under tensional failure: Apparent strengthening by dilatancy, *J. Geophys. Res.*, *97*, 273–286, doi:10.1029/91JB02256.
- Shimamoto, T., and J. M. Logan (1981), Effects of simulated clay gouges on the sliding behavior of Tennessee sandstone, *Tectonophysics*, *75*, 243–255.
- Summers, R., and J. Byerlee (1977a), A note on the effect of fault gouge composition on the stability of frictional sliding, *Int. J. Rock Mech. Min. Sci.*, *14*, 155–160.
- Summers, R., and J. Byerlee (1977b), Summary of results of frictional sliding studies, at confining pressures up to 6.98 kb, in selected rock materials, *U.S. Geol. Surv. Open File Rep.*, *77-142*, 129 pp.
- Takahashi, M., K. Mizoguchi, K. Kitamura, and K. Masuda (2007), Effects of clay content on the frictional strength and fluid transport property of faults, *J. Geophys. Res.*, *112*, B08206, doi:10.1029/2006JB004678.
- Tembe, S., D. A. Lockner, and T.-F. Wong (2010), Effect of clay content and mineralogy on frictional sliding behavior of simulated gouges: Binary and ternary mixtures of quartz, illite and montmorillonite, *J. Geophys. Res.*, *115*, B03416, doi:10.1029/2009JB006383.
- Wang, C.-Y. (2011), High pore pressure, or its absence, in the San Andreas fault, *Geology*, *39*(11), 1047–1050.

- Wang, C.-Y., N.-H. Mao, and F. T. Wu (1980), Mechanical properties of clays at high pressure, *J. Geophys. Res.*, *85*, 1462–1468, doi:10.1029/JB085iB03p01462.
- Warkentin, B. P., and R. N. Yong (1962), Shear strength of montmorillonite and kaolinite related to interparticle forces, in *Clays and Clay Minerals: Proc. 9th National Conf.*, edited by A. Swineford, pp. 210–218, Pergamon Press, Oxford, U. K.
- Wibberley, C. A. J. (2002), Hydraulic diffusivity of fault gouge zones and implications for thermal pressurization during seismic slip, *Earth Planet. Space*, *54*, 1153–1171, doi:10.1186/BF03353317.